LASER TECHNOLOGIES

PACS numbers: 42.55.Px; 42.60.Jf
DOI: 10.1070/QE2010v040n05ABEH013976

Radiation transfer in metallic-powder beds during laser forming

A.V. Gusarov

Abstract. **This paper presents numerical simulations of two-dimensional radiation transfer in a powder layer that resides on a substrate of the same material and is exposed to a normally incident laser beam with an axisymmetric bell-shaped or top-hat intensity profile. The powder layer is treated as an equivalent homogeneous absorbing/scattering medium with radiative properties defined by the reflectance of the solid phase, the porosity of the powder and its surface area. The model used is applicable when the laser beam diameter far exceeds the particle size of the powder. It is shown that the absorptance of an optically thick layer of opaque powder particles is a universal function of the absorptance of the solid phase and is independent of surface area and porosity, in agreement with experimental data in the literature. The fraction of laser energy absorbed in the powder-substrate system and that absorbed in the substrate decrease with an increase in the reflectance of the material, but the powder bed is then more uniformly heated.**

Keywords: *selective laser sintering, selective laser melting, radiation transfer equation.*

1. Introduction

Scanning a powder bed with a laser beam is a basic operation in a variety of additive forming processes, such as selective laser sintering or selective laser melting (SLM) [1]. In a typical SLM geometry, a laser beam is incident on a powder bed along the normal to the substrate surface [2]. In layerwise forming processes, thin powder layer deposition and laser scanning are repeated many times, so that each powder layer is applied to a substrate formed by the underlying melted layers. Such a geometry (powder layer/substrate) is also typical of laser cladding with preplaced powder [3]. The incident laser radiation penetrates into the powder through open pores [4] and delivers energy directly to its bulk and to the substrate [2]. Radiative energy transfer may prevail over heat conduction at a low thermal conductivity of the powder [5], so the spatial distribution of the deposited energy directly influences the local temperature field [2].

Questions of major importance in laser processing are the incident intensity loss distribution over backscattering and absorption channels in the powder and substrate, the through-thickness uniformity of energy deposition in the powder and the broadening of the 'energy deposition spot' relative to the laser beam projection. The reflectance of the powder-substrate system is directly related to the energy efficiency of the process. Increasing the fraction of laser radiation absorbed directly by the substrate is favourable for metallurgical bonding between the melted powder and substrate [2]. Improving the through-thickness uniformity of energy deposition allows one to avoid surface overheating and, hence, to reduce vaporisation losses. The depth and width of the laser energy deposition zone are directly related to the spatial resolution of the laser forming process.

Experimental studies of laser light reflection from powder beds [6, 7] have shown that, in the case of highly reflective materials (metals), the surface absorptance of a powder bed considerably exceeds that of a smooth surface of the same material. Theoretical analysis using computer simulation of ray propagation [8] and a homogenised radiation transfer equation (RTE) [4, 7] has shown that there is a universal relation between the normal-incidence absorptance of a powder and the absorptance of a smooth surface of the same material. Experimental data available in the literature are, on the whole, consistent with this relation [7]. As pointed out by Van der Scheuren [9], laser radiation penetrates into the powder bed rather than being absorbed by the surface. In his work, the deposited-energy depth profile was assessed using form factors. Similar profiles were obtained using ray-optics analysis [8] and the RTE [4]. The theoretical laser light penetration depth in powder was confirmed experimentally [10].

Radiation transfer in optically thick powder beds has been analysed in detail [4, 7 – 9], whereas thin layers have been the subject of only a few simulation studies, with perfectly [4] and partially [7] reflective substrates examined. Those theoretical studies relied on one-dimensional (1D) models, incapable of assessing the radial profile of the deposited energy. This work examines radiation transfer in 2D cylindrical geometry in a powder bed on a solid substrate of the same material.

2. Model

The problem of an axisymmetric laser beam incident on a powder layer along the normal to its surface is analysed

A.V. Gusarov A.A. Baikov Institute of Metallurgy and Materials Science, Russian Academy of Sciences, Leninsky prosp. 49, 119991 Moscow, Russia; e-mail: AV.Gusarov@relcom.ru

Received 1 October 2008; revision received 28 January 2009
Kvantovaya Elektronika **40** (5) 451 – 459 (2010)
Translated by O.M. Tsarev

here in cylindrical coordinates. The beam axis, z, is directed along the inward normal to the powder surface (Fig. 1a). The powder, consisting of opaque particles, can be thought of as an equivalent homogeneous absorbing/scattering medium, and light propagation in this medium can be described using the conventional RTE [11]. The radiation intensity at point M with coordinates (z, r) (Fig. 1b) can then be characterised by its average, $I(\boldsymbol{\Omega})$, where $\boldsymbol{\Omega}$ is a unit vector in the light propagation direction, defined by a polar angle (θ) and azimuth (φ) as illustrated in Fig. 1b. The azimuth angle is measured not from a fixed direction but from the plane passing through point M and the z axis. In these coordinates, the RTE has the form [12]

$$\cos\theta\,\frac{\partial I}{\partial z}+\frac{\sin\theta}{r}\left\{\cos\varphi\,\frac{\partial(rI)}{\partial r}-\frac{\partial(I\sin\varphi)}{\partial\varphi}\right\}$$

$$=-\beta I+\frac{\sigma}{2\pi}\int_0^{\pi}\mathrm{d}\varphi'\int_{-1}^{1}P(\theta,\varphi,\theta',\varphi')I(\theta',\varphi')\mathrm{d}\cos\theta', \quad (1)$$

where the extinction coefficient β, scattering coefficient σ and scattering phase function $P(\boldsymbol{\Omega},\boldsymbol{\Omega}')$ [describes the intensity scattered in the $\boldsymbol{\Omega}'(\theta',\varphi')$ direction when the initial propagation direction is $\boldsymbol{\Omega}(\theta,\varphi)$] are effective radiative characteristics of the powder layer.

The boundary condition on the powder surface ($z = 0$) is set by the intensity of normally incident collimated radiation with an energy flux density $Q_0(r)$:

$$I(\theta,\varphi)=\frac{Q_0}{2\pi}\,\delta(\cos\theta-1),\quad \theta<\pi/2\,, \quad (2)$$

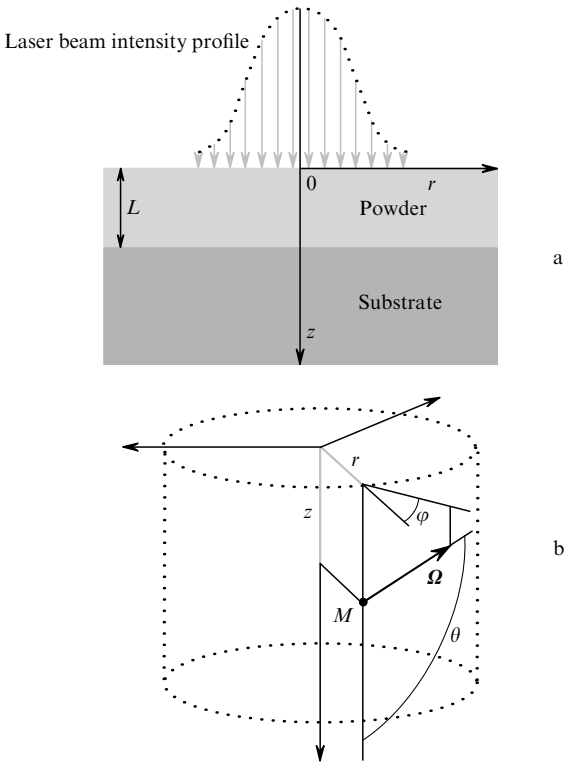

Figure 1. Geometry of the problem of radiation transfer in a powder layer of thickness L on a partially reflective, opaque substrate: (a) cylindrical coordinates; (b) light propagation direction in the substrate, $\boldsymbol{\Omega}$, defined by a polar angle and azimuth at point M.

where δ is the Dirac delta function. The substrate surface ($z = L$) is assumed to be specular, with reflectance ρ:

$$I(\theta,\varphi)=\rho I(\pi-\theta,\varphi),\quad \theta>\pi/2. \quad (3)$$

2.1 Effective radiative properties of a powder bed

According to general homogenisation theory [11], the effective extinction coefficient of a statistically isotropic packed bed of opaque particles is given by

$$\beta=\frac{S}{4f_0}, \quad (4)$$

where S is the surface area per unit volume of the packed bed and f_0 is its porosity (the volume fraction of open spaces). If the powder consists of n particle species (n opaque phases) with a known particle surface to volume ratio, S_α, for each species (surface area per unit volume of phase α), we have

$$S=\sum_{\alpha=1}^{n}S_\alpha f_\alpha, \quad (5)$$

where f_α is the volume fraction of phase α. Metallic powders prepared by atomisation processing [1], as are widely used in laser forming, can be considered a mixture of several size fractions, each consisting of spherical particles of diameter D_α. Therefore,

$$S_\alpha=\frac{6}{D_\alpha}. \quad (6)$$

For packed beds of monodisperse opaque spheres, we obtain from Eqns (4)–(6)

$$\beta=\frac{3}{2}\,\frac{1-f_0}{f_0 D_1}. \quad (7)$$

The effective scattering coefficient σ and scattering phase function P of a statistically isotropic one-component powder consisting of specular opaque particles can be estimated as [11]

$$\frac{\sigma}{\beta}=\rho_1,\quad P=\frac{\rho_1'}{\rho_1}, \quad (8)$$

where ρ_1 is the hemispherical reflectance and ρ_1' is the directional reflectance (see Siegel and Howell [13] for definitions). Relations (8) can be generalised to a mixture of n opaque phases with different ρ_α and ρ_α' by averaging with weights proportional to the surface area of each phase [4]:

$$\frac{\sigma}{\beta}=\frac{1}{S}\sum_{\alpha=1}^{n}\rho_\alpha S_\alpha f_\alpha,\quad P\,\frac{\sigma}{\beta}=\frac{1}{S}\sum_{\alpha=1}^{n}\rho_\alpha' S_\alpha f_\alpha. \quad (9)$$

The directional reflectance ρ_α' of widely used metals, such as Fe, Al and Cu, and many other highly reflective materials is a weak function of the angle of incidence, except at grazing incidence. Consequently, the scattering phase function depends little on scattering angle except at small angles (see Gusarov et al. [7] for examples). Therefore, the isotropic phase function

$$P = 1 \tag{10}$$

provides a good approximation.

2.2 Numerical method

The radiation transfer equation (1) was solved numerically using the discrete ordinates method. The light propagation direction is defined by the parameters $\mu = \cos\theta$ and φ. The region $(-1 < \mu < 1,\ 0 < \varphi < \pi)$ is divided into $N_\mu \times N_\varphi$ identical rectangular cells of dimensions $\Delta\mu \times \Delta\varphi$ ($\Delta\mu = 2/N_\mu$, $\Delta\varphi = \pi/N_\varphi$), centred at the points defined by $\mu_k = (k + 1/2)\Delta\mu - 1$ and $\varphi_l = (l + 1/2)\Delta\varphi$, with $k = 0, \ldots,\ N_\mu - 1$ and $l = 0, \ldots,\ N_\varphi - 1$. Integrating Eqn (1) over cell (k, l), we obtain

$$\begin{aligned}
&\frac{\partial}{\partial z}\int_{\varphi_l-\Delta\varphi/2}^{\varphi_l+\Delta\varphi/2} \mathrm{d}\varphi \int_{\mu_k-\Delta\mu/2}^{\mu_k+\Delta\mu/2} rI(\mu,\varphi)\mu \mathrm{d}\mu \\
&\quad + \frac{\partial}{\partial r}\int_{\varphi_l-\Delta\varphi/2}^{\varphi_l+\Delta\varphi/2} \cos\varphi \mathrm{d}\varphi \int_{\mu_k-\Delta\mu/2}^{\mu_k+\Delta\mu/2} rI(\mu,\varphi)\sqrt{1-\mu^2}\mathrm{d}\mu \\
&+ \int_{\mu_k-\Delta\mu/2}^{\mu_k+\Delta\mu/2} [\sin(\varphi_l - \Delta\varphi/2) I(\mu, \varphi_l - \Delta\varphi/2) - \sin(\varphi_l + \Delta\varphi/2) \\
&\quad \times I(\mu, \varphi_l + \Delta\varphi/2)]\sqrt{1-\mu^2}\mathrm{d}\mu = -\beta \int_{\varphi_l-\Delta\varphi/2}^{\varphi_l+\Delta\varphi/2} \mathrm{d}\varphi \\
&\quad \times \int_{\mu_k-\Delta\mu/2}^{\mu_k+\Delta\mu/2} rI(\mu,\varphi)\mu \mathrm{d}\mu + \frac{\sigma}{2\pi}\sum_{k'=0}^{N_\mu-1}\sum_{l'=0}^{N_\varphi-1} \int_{\varphi_l-\Delta\varphi/2}^{\varphi_l+\Delta\varphi/2} \mathrm{d}\varphi \\
&\quad \times \int_{\mu_k-\Delta\mu/2}^{\mu_k+\Delta\mu/2} \mathrm{d}\mu \int_{\varphi_{l'}-\Delta\varphi/2}^{\varphi_{l'}+\Delta\varphi/2} \mathrm{d}\varphi' \int_{\mu_{k'}-\Delta\mu/2}^{\mu_{k'}+\Delta\mu/2} rI(\mu', \varphi') \\
&\quad \times P(\theta, \varphi, \theta', \varphi')\mathrm{d}\mu',
\end{aligned} \tag{11}$$

where the scattering integral is represented as the sum of the integrals over the cells. The angular intensity term $I(\mu, \varphi)$ is assumed to vary little within a given cell, so it can be replaced, to second-order accuracy, by its average, I_{kl}. Equation (1) can thus be approximated to second-order accuracy by the system of linear transfer equations

$$\begin{aligned}
&\mu_k \frac{\partial(rI_{kl})}{\partial z} + \cos\varphi_l\sqrt{1-\mu_k^2}\,\frac{\partial(rI_{kl})}{\partial r} + \sqrt{1-\mu_k^2} \\
&\quad \times \frac{\sin\varphi_{l-1/2}I_{kl-1/2} - \sin\varphi_{l+1/2}I_{kl+1/2}}{\Delta\varphi} = -\beta r I_{kl} \\
&\quad + \frac{\sigma}{2\pi N_\mu N_\varphi}\sum_{k'=0}^{N_\mu-1}\sum_{l'=0}^{N_\varphi-1} P_{klk'l'} r I_{k'l'},
\end{aligned} \tag{12}$$

where the scattering matrix is given by

$$\begin{aligned}
P_{klk'l'} &= \frac{1}{(\Delta\mu\Delta\varphi)^2}\int_{\varphi_l-\Delta\varphi/2}^{\varphi_l+\Delta\varphi/2} \mathrm{d}\varphi \int_{\mu_k-\Delta\mu/2}^{\mu_k+\Delta\mu/2} \mathrm{d}\mu \\
&\quad \times \int_{\varphi_{l'}-\Delta\varphi/2}^{\varphi_{l'}+\Delta\varphi/2} \mathrm{d}\varphi' \int_{\mu_{k'}-\Delta\mu/2}^{\mu_{k'}+\Delta\mu/2} P(\theta, \varphi, \theta', \varphi')\mathrm{d}\mu'.
\end{aligned} \tag{13}$$

It can be found by numerically integrating (13) over the (μ_k, φ_l) grid and is then used to numerically solve Eqns (12).

System (12) can be solved numerically using iterations modelling unsteady-state transfer; i.e., the unsteady-state transfer equations

$$\begin{aligned}
&\frac{\partial(rI_{kl})}{\partial t} + \mu_k \frac{\partial(rI_{kl})}{\partial z} + \cos\varphi_l\sqrt{1-\mu_k^2}\,\frac{\partial(rI_{kl})}{\partial r} + \sqrt{1-\mu_k^2} \\
&\quad \times \frac{\sin\varphi_{l-1/2}I_{kl-1/2} - \sin\varphi_{l+1/2}I_{kl+1/2}}{\Delta\varphi} = -\beta r I_{kl} \\
&\quad + \frac{\sigma}{2\pi N_\mu N_\varphi}\sum_{k'=0}^{N_\mu-1}\sum_{l'=0}^{N_\varphi-1} P_{klk'l'} r I_{k'l'}
\end{aligned} \tag{14}$$

involving the time variable t, can be solved with initial conditions of zero, $I_{kl} = 0$, in the cylindrical region of radius $R_{\max}$ $(0 < z < L,\ 0 < r < R_{\max})$. The t variable corresponds to the product of time with the 'speed of light' in an imaginary unsteady-state process and has the dimensions of length. A steady-state solution to Eqns (14) must meet Eqns (12).

Let us introduce a uniform grid $(z^{(i)} = i\Delta z,\ r^{(j)} = j\Delta r)$, where $i = 0, \ldots, M_z$ and $j = 0, \ldots, M_r$, with grid spacings $\Delta z = L/M_z$ and $\Delta r = R_{\max}/M_r$. Equations (14) are approximated using a conservative implicit scheme accurate to second order in space and to first order in t:

$$\begin{aligned}
&\frac{r^{(j)}I_{kl}^{(i,j)}(t+\Delta t) - r^{(j)}I_{kl}^{(i,j)}(t)}{\Delta t} \\
&\quad + \mu_k \frac{r^{(j)}I_{kl}^{(i+1/2,j)}(t) - r^{(j)}I_{kl}^{(i-1/2,j)}(t)}{\Delta z} \\
&\quad + \cos\varphi_l\sqrt{1-\mu_k^2}\,\frac{(rI)_{kl}^{(i,j+1/2)}(t) - (rI)_{kl}^{(i,j-1/2)}(t)}{\Delta r} \\
&\quad + \sqrt{1-\mu_k^2}\,\frac{\sin\varphi_{l-1/2}I_{kl-1/2}^{(i,j)}(t) - \sin\varphi_{l+1/2}I_{kl+1/2}^{(i,j)}(t)}{\Delta\varphi} \\
&= -\beta r^{(j)}I_{kl}(i,j)(t) + \frac{\sigma}{2\pi N_\mu N_\varphi}\sum_{k'=0}^{N_\mu-1}\sum_{l'=0}^{N_\varphi-1} P_{klk'l'} r^{(j)} I_{k'l'}^{(i,j)}(t),
\end{aligned} \tag{15}$$

where Δt is the t increment, and the discrete intensity $I_{kl}^{(i,j)}$ at node (i, j) is the average $I_{kl}(z, r)$ over the toroidal region with $z = z^{(i)} - \Delta z/2, \ \ldots, z^{(i)} + \Delta z/2$ and $r = r^{(j)} - \Delta r/2, \ldots, r^{(j)} + \Delta r/2$. The values with half-integer i and j can be found by the minmod slope-limiter method [14]. Typical grid dimensions in this study are $N_\mu = 128$, $N_\varphi = 32$, $M_z = 20$ and $M_r = 50$. To ensure stability of the implicit scheme (15), Δt is estimated using the Courant condition [14].

2.3 One-dimensional approximation

If the incident beam is broad enough and the incident power density, Q_0 in (2), is a weak function of radial coordinate r, the intensity I varies little with r and φ, and the second term on the right-hand side of (1) can be neglected. This leads to a spatially homogeneous (1D) RTE. Such a quasi-1D model can be treated using the numerical method described in Gusarov et al. [7]. A numerical 1D model is needed to explore directional radiative characteristics, e.g. directional reflectance [7], although sufficiently accurate integral characteristics of radiation transfer, e.g.

hemispherical reflectance, can be obtained in the four-moment analytical approximation proposed earlier [4] for the 1D RTE.

The solution to the 1D RTE

$$\mu \frac{\partial I(z,\mu)}{\partial z} = \beta\left[\frac{\omega}{2}\int_{-1}^{1} I(z,\mu')P(\mu',\mu)\mathrm{d}\mu' - I(z,\mu)\right] \quad (16)$$

(where ω is the scattering albedo) that meets the boundary conditions (2) and (3) is approximated by a four-parameter function [4] of the form

$$I(z,\mu) = \frac{Q_+(z)}{2\pi}\,\delta(\mu-1) + \frac{Q_-(z)}{2\pi}\,\delta(\mu+1) + F(z,\mu). \quad (17)$$

Here Q_+ and Q_- are the incident and backscattered collimated radiation flux densities, corresponding to the incident and reflected beams, and F is the diffuse intensity resulting from (multiple) scattering of the collimated components. Substituting (17) into (16) and using the boundary conditions (2) and (3), we obtain a separate problem for the collimated components [4],

$$\frac{\mathrm{d}Q_+}{\mathrm{d}z} = -\beta Q_+, \quad \frac{\mathrm{d}Q_-}{\mathrm{d}z} = \beta Q_-, \qquad Q_+(0) = Q_0, \;\; Q_-(L) = \rho Q_+(L) \quad (18)$$

with the solution

$$Q_+ = Q_0\exp(-\xi), \quad Q_- = \rho Q_0\exp(\xi - 2\Lambda) \quad (19)$$

(where $\xi = \beta z$ is a nondimensional coordinate and $\Lambda = \beta L$ is the optical thickness of the powder bed), and a boundary value problem describing diffuse radiation [4]:

$$\mu \frac{\partial F(z,\mu)}{\partial z} = \frac{\beta\omega}{4\pi}[Q_+(z)P(1,\mu) + Q_-(z)P(-1,\mu)] + \beta\left[\frac{\omega}{2}\int_{-1}^{1} F(z,\mu')P(\mu',\mu)\mathrm{d}\mu' - F(z,\mu)\right], \quad (20)$$

$$F(0,\mu) = 0 \text{ for } \mu > 0, \;\; F(L,\mu) = \rho F(L,-\mu) \text{ for } \mu < 0. \quad (21)$$

In the two-flux method, an approximate solution to Eqns (20) and (21) is sought in the form

$$F(z,\mu) = F_+(z)h(\mu) + F_-(z)[1-h(\mu)], \quad (22)$$

where h is the Heaviside step function. In the case of isotropic scattering [see (10)], substitution of (22) into Eqn (20) and integration over the ranges $0 < \mu < 1$ and $-1 < \mu < 0$ give two moment equations for the nondimensional coefficients $f_\pm = 2\pi F_\pm/Q_0$,

$$\pm\frac{1}{2}\frac{\mathrm{d}f_\pm}{\mathrm{d}\xi} = \frac{\omega}{2}(q_+ + q_- + f_+ + f_-) - f_\pm, \quad (23)$$

which contain the nondimensional functions $q_+ = Q_+/Q_0 = \exp(-\xi)$ and $q_- = Q_-/Q_0 = \rho\exp(\xi - 2\Lambda)$. The boundary conditions for $f_\pm$ follow from (21):

$$f_+(0) = 0, \quad f_-(\Lambda) = \rho f_+(\Lambda). \quad (24)$$

The general solution to (23) can be obtained from the relations

$$f_+ + f_- = C_1\exp(-2a\xi) + C_2\exp(2a\xi) - \frac{4\omega[\exp(-\xi) + \rho\exp(\xi - 2\Lambda)]}{4\omega - 3}, \quad (25)$$

$$f_+ - f_- = aC_1\exp(-2a\xi) - aC_2\exp(2a\xi) - \frac{2\omega[\exp(-\xi) - \rho\exp(\xi - 2\Lambda)]}{4\omega - 3}, \quad (26)$$

where $a = \sqrt{1-\omega}$. The constants C_1 and C_2 can be found from the boundary conditions (24):

$$C_1 = 2\omega\,\frac{(1-a)(1-\rho^2)\exp(-\Lambda)}{(4\omega-3)D} - \frac{[1+a-\rho(1-a)\exp(2a\Lambda)(3+\rho\exp(-2\Lambda)}{(4\omega-3)D}, \quad (27)$$

$$C_2 = 2\omega\,\frac{[1-a-\rho(1+a)]\exp(-2a\Lambda)[3+\rho\exp(-2\Lambda)]}{(4\omega-3)D} - \frac{(1+a)-(1-\rho^2)\exp(-\Lambda)}{(4\omega-3)D}, \quad (28)$$

$$D = (1-a)[1-a-\rho(1+a)]\exp(-2a\Lambda) - (1+a)[1+a-\rho(1-a)]\exp(2a\Lambda). \quad (29)$$

3. Results and discussion

The effect of radiation transfer on thermal processes [2] can be described using the radiant flux density, $\boldsymbol{Q}$, with the components

$$Q_z = 2\int_0^\pi \mathrm{d}\varphi\int_{-1}^{1} I\cos\theta\,\mathrm{d}\cos\theta, \qquad Q_r = 2\int_0^\pi \cos\varphi\,\mathrm{d}\varphi\int_{-1}^{1} I\sin\theta\,\mathrm{d}\cos\theta \quad (30)$$

and the volumetric heat source

$$U = -\mathrm{div}\boldsymbol{Q} = -\frac{\partial Q_z}{\partial z} - \frac{1}{r}\frac{\partial(rQ_r)}{\partial r}. \quad (31)$$

These parameters can be obtained by numerically treating the numerical solution to (1). In the 1D model, $Q_r = 0$ and Q_z can be derived from the general solution (25)–(29):

$$q_z(\xi) = \frac{Q_z}{Q_0} = \frac{f_+ - f_-}{2} + q_+ - q_- = \frac{\omega a}{(4\omega-3)D} \times\{(1-\rho^2)\exp(-\Lambda)[(1-a)\exp(-2a\xi) + (1+a)\exp(2a\xi)] - [3+\rho\exp(-2\Lambda)]\{[1+a-\rho(1-a)]\exp[2a(\Lambda-\xi)] + [1-a-\rho(1+a)]\exp[2a(\xi-\Lambda)]\}\} -$$

$$- \frac{3(1-\omega)[\exp(-\xi) - \rho\exp(\xi - 2\Lambda)]}{4\omega - 3}. \quad (32)$$

3.1 Absorptance of optically thick powder beds

Absorptance, A, is the ratio of the radiant flux density (30) across a surface to the incident radiant flux density. In the case of a flat surface under uniform irradiation, this ratio is equal to the normalised component $q_z(0)$ (32) in the 1D analytical model. In the optically thick limit, we have

$$A = \lim_{\Lambda\to\infty} q_z(0) = \frac{3a}{1+2a}. \quad (33)$$

Numerical solutions to the RTE [7] for normal incidence and isotropic scattering demonstrate high accuracy of this analytical solution. According to (33), the absorptance of an optically thick powder bed depends only on its albedo, ω, because $a = \sqrt{1-\omega}$. The absorptance is independent of particle morphology and powder density.

It follows from homogenisation theory [11] that the albedo, ω, of a statistically isotropic packed bed of opaque particles is equal to the hemispherical reflectance, ρ_1, of the solid phase [see (8)]. Therefore, the absorptance can be expressed directly through ρ_1 or the absorptance, $1-\rho_1$, of the solid phase:

$$A = \frac{3\sqrt{1-\rho_1}}{1+2\sqrt{1-\rho_1}}. \quad (34)$$

This function is shown in Fig. 2. The experimental data presented in Fig. 2 are seen to be on the whole consistent with the theoretical prediction. The deviations of the data points from the theoretical curve, related to experimental conditions, were analysed elsewhere [4, 6, 7].

Attempts to analyse the surface absorptance of powder beds were also made earlier. In particular, using Monte Carlo simulation in an absorbing/scattering medium approximation [15], it was shown to depend on transport albedo. The next step was the recognition that the albedo of a one-component powder can be evaluated from the absorptance of a smooth surface of the same material [7]. Basically the same theoretical curve, obtained by a different method, is shown in Fig. 2. The curve is compared to experimental data from different studies for various porosities. As seen, the absorptance of a powder bed does correlate with that of a smooth surface of the same material, as predicted theoretically.

3.2 Absorptance of an optically thick powder bed on a substrate

The absorptance of a powder-substrate system, A, and the fraction of radiation absorbed in the substrate, A_s, can be obtained from the function $q_z(\xi)$ in (32):

$$A = q(0) = \frac{\omega a}{(4\omega-3)D}\{2(1-\rho^2)\exp(-\Lambda)$$

$$-[3+\rho\exp(-2\Lambda)]\{[1+a-\rho(1-a)]\exp(2a\Lambda) \quad (35)$$

$$+[1-a-\rho(1+a)]\exp(-2a\Lambda)\}\} - \frac{3(1-\omega)[1-\rho\exp(-2\Lambda)]}{4\omega-3},$$

$$A_s = q(\Lambda) = \frac{\omega a}{(4\omega-3)D}\{(1-\rho^2)\exp(-\Lambda)$$

$$\times[(1-a)\exp(-2a\Lambda) + (1+a)\exp(2a\Lambda)] - 2(1-\rho)$$

$$\times[3+\rho\exp(-2\Lambda)]\} - \frac{3(1-\omega)(1-\rho)\exp(-\Lambda)}{4\omega-3}. \quad (36)$$

Figure 3 shows the fraction of absorbed energy as a function of the absorptance of the solid phase for a powder bed and a substrate of the same material. The absorptance A rises steadily as a function of the optical thickness of the powder bed, Λ, approaching the limit given by (34) (see the curve in Fig. 2).

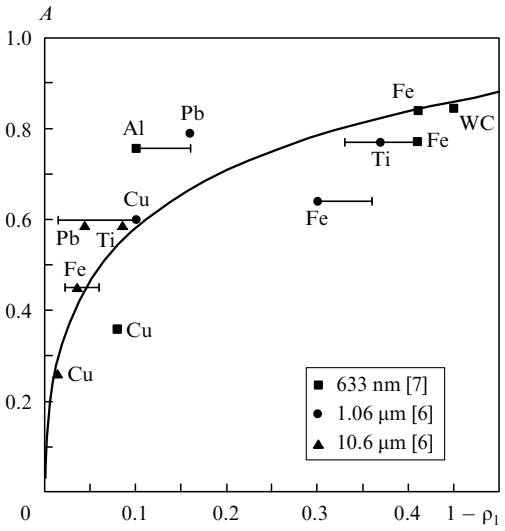

Figure 2. Absorptance, A, of an optically thick powder bed against the absorptance of the solid phase, $1-\rho_1$. The solid line shows the theoretical curve and the points represent experimental data for micron-sized particles at different wavelengths.

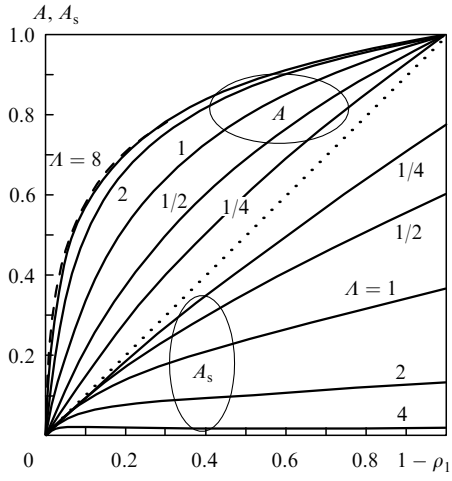

Figure 3. Fraction of absorbed laser radiation as a function of the absorptance of the solid phase, $1-\rho_1$, for a powder bed and substrate of the same material (A) and the substrate (A_s) at different optical thicknesses of the powder bed, Λ. The dotted line represents the limit of the substrate with no powder.

Thus, the energy efficiency of the laser processing of a substrate covered with a powder bed of the same material always exceeds that of the substrate without powder and increases with bed thickness. The physical interpretation of this effect is that the surface of an uncovered substrate reflects the incident laser radiation only once. In the case of a porous coating, some of the incident radiation penetrates into pores and experiences multiple reflection. Since each reflection event is accompanied by absorption of some energy, the net fraction absorbed increases. Nevertheless, the absorbed energy has a nonuniform depth profile in the powder, and the fraction of radiation that reaches the substrate, A_s, decreases monotonically with increasing Λ (Fig. 3), which is undesirable because it may lead to the melting of only the top layer of the powder bed, with no metallurgical bonding to the substrate. Heating and melting of the substrate are often thought to be necessary conditions for high-quality laser processing. Note that, at large optical thicknesses, A_s as a function of ρ_1 has a local maximum (see e.g. the $\Lambda = 4$ curve in Fig. 3). This suggests that, varying the laser wavelength, one can raise A_s because the ρ_1 of a given material is a function of wavelength.

3.3 Effect of the radial intensity profile of the incident beam

Figure 4 illustrates the effect of the radial intensity profile of the incident laser beam on radiation transfer in a powder bed. A bell-shaped beam profile is compared to two top-hat profiles. The width of the broad top-hat beam is equal to the full width of the bell-shaped profile, and that of the narrow top-hat beam, to the full width at half maximum of the bell. The energy flux densities in Figs 4a–4c are normalised to the maximum incident radiant flux density: $q_z = Q_z/Q_0$, $q_r = Q_r/Q_0$. The absorbed energy in Fig. 4d is normalised as follows: $u = U/(\beta Q_0)$.

The axial energy flux density, q_z, in the powder (Fig. 4b) reaches a maximum on the surface. Because of the backscattering, the height of the maximum is considerably lower than the incident energy flux density. The axial flux density on the surface is negative beyond the beam spot, where the incident intensity is zero, but there is the backscattered radiation. The attenuation of q_z with increasing depth, z, is caused by absorption. The radial flux q_r (Fig. 4c), characterising transverse energy transfer, has a maximum at the periphery of the laser beam. The weak tails in the deposited-energy profiles beyond the beam spot (Fig. 4d) are due to the radial transfer.

The above features are clearly seen in 1D sections of the 2D profiles in Fig. 5, which compares the rigorous 2D description of radiation transfer using Eqn. (1) and the 1D approximation, which neglects the radial component Q_r of the energy flux density. The curves in Fig. 5 illustrate the results obtained in the analytical 1D two-flux model. With the parameters under consideration, the 2D and 1D models differ not very much. The broadening of the profile is most pronounced for the narrow top-hat beam (Fig. 5b). The reduction in the energy deposited on the axis, due to the transverse radiation transfer, is appreciable for the bell-shaped and narrow top-hat beams (Fig. 5c).

The thermal conditions of laser processing depend on

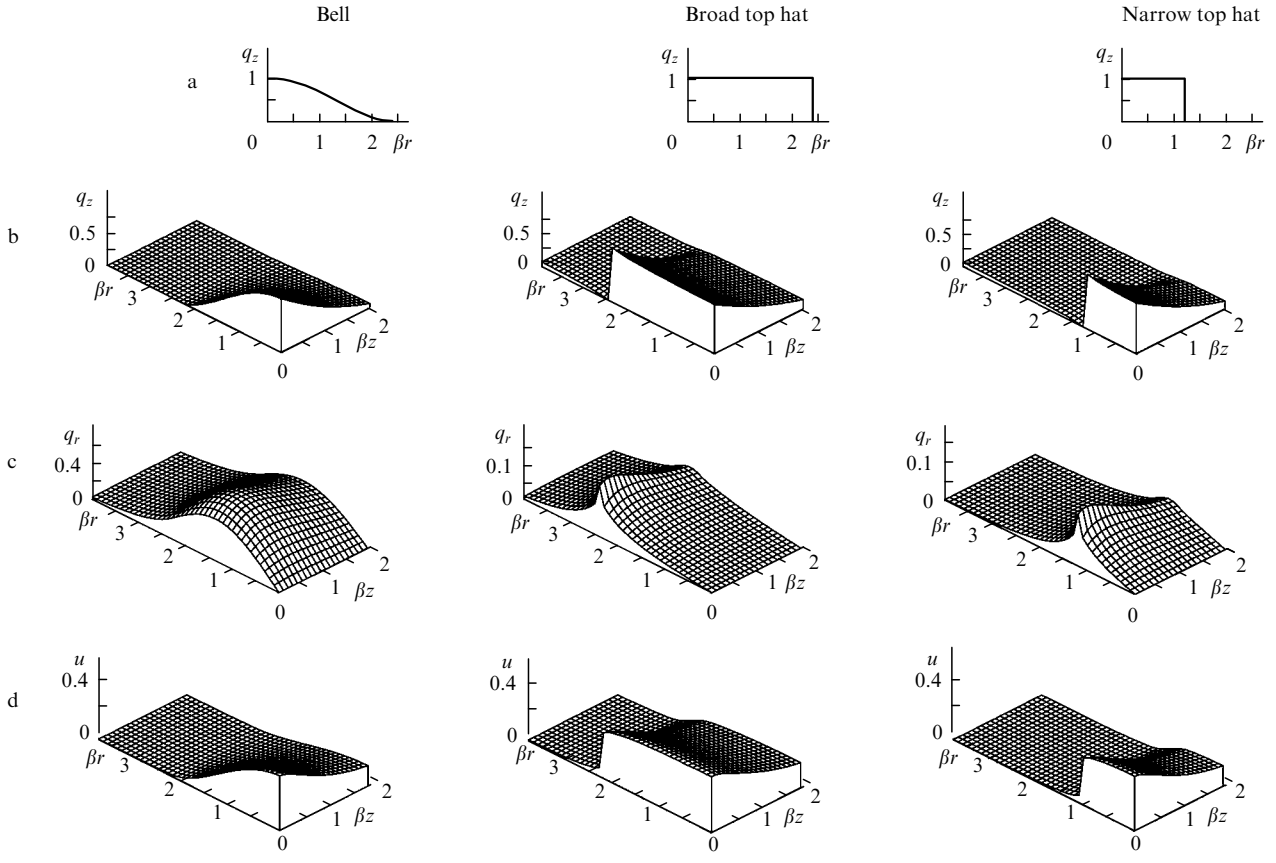

Figure 4. 2D laser radiation transfer in a powder bed of optical thickness $\Lambda = 2$ and albedo $\omega = \rho_1 = \rho = 0.7$: (a) radial profiles of the incident laser power density; (b) normalised axial energy flux density, q_z; (c) normalised radial energy flux density, q_r; (d) normalised absorbed energy, u.

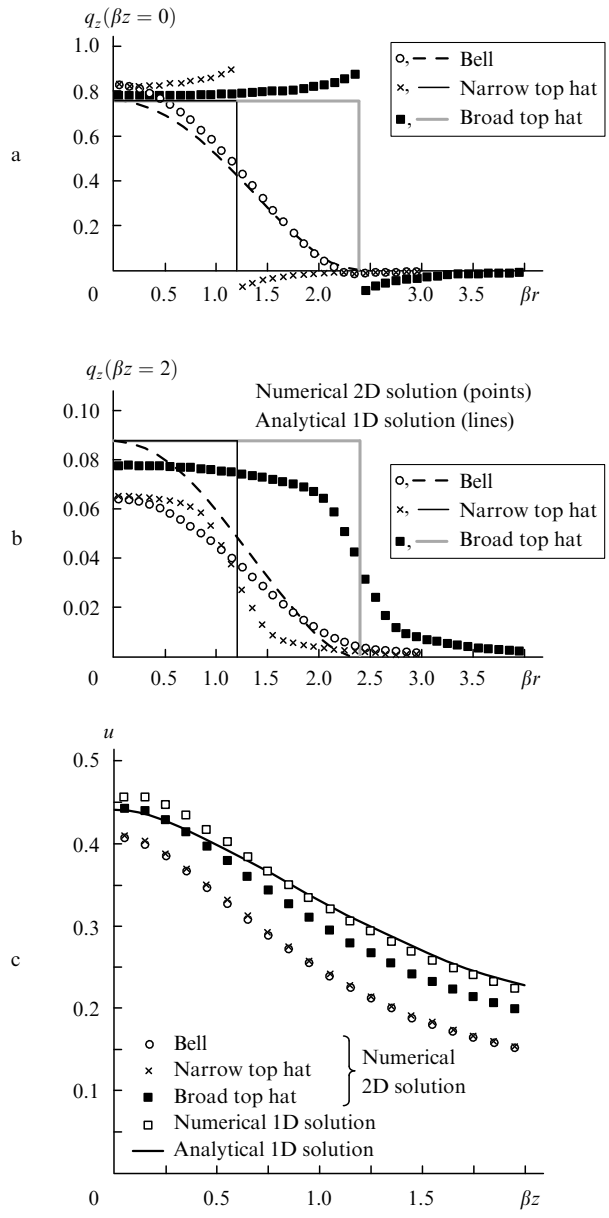

Figure 5. Comparison of the radiative transfer in a powder bed of optical thickness $\Lambda = 2$ and albedo $\omega = \rho_1 = \rho = 0.7$ for bell-shaped (half width at half maximum $\beta r = 1.2$), narrow top-hat ($\beta r = 1.2$) and broad top-hat ($\beta r = 2.4$) laser beams: (a, b) normalised axial energy flux density, q_z, on the powder and substrate surfaces, respectively; (c) normalised absorbed energy on the axis, u.

the energy flux across the substrate surface (Fig. 5b) and the volumetric heat source (Fig. 5c). Comparison of the 1D and 2D approximations for the relatively narrow laser beams under consideration indicates that the radial transfer of radiant energy can considerably reduce both the energy flux and the volumetric source at the beam centre, whereas the broadening of the radial profile of the deposited energy is less significant. For this reason, when the incident beam has a bell-shaped profile, the divergence of the scattered laser light in the powder leads to the formation of weak tails in the deposited-energy profile beyond the beam spot (circles and dashed curve in Fig. 5b). The broadening of top-hat profiles can be thought of as smoothing of the lateral beam profile boundary (crosses, thin line, squares and heavy line in Fig. 5b). The maximum temperature, which occurs at the beam axis, is assumed to be lowered by the radial transfer, whereas the corresponding rise in temperature beyond the beam spot will be insufficient to cause any structural or phase changes.

3.4 Effect of the reflectance of the solid phase

The reflectance of a material, $\rho_1 = \rho = \omega$, and the corresponding albedo of powder, ω, can be tuned by varying, e.g., the laser wavelength. This is illustrated in Figs 6 and 7 for a fixed bell-shaped radial laser beam profile. A general trend is that, with increasing reflectance, ρ, the depth profile of the absorbed energy, U, becomes more uniform (Fig. 6), whereas its peak value decreases considerably. According to Fig. 6, the effect of reflectance

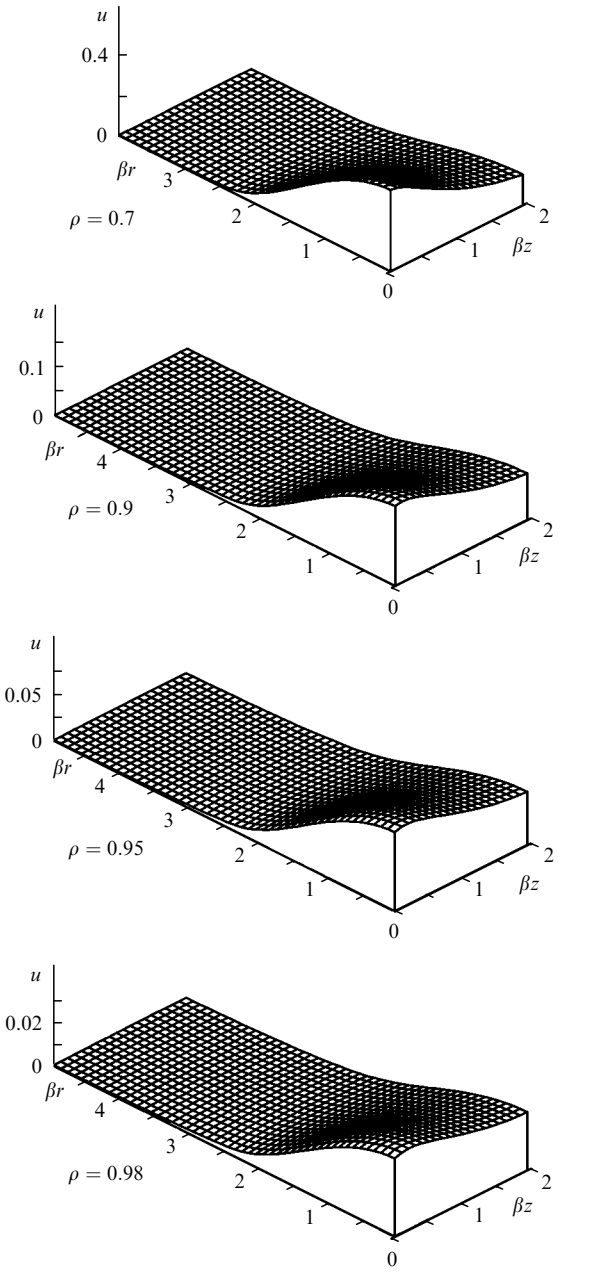

Figure 6. 2D profiles of normalised absorbed energy, u, in powder beds of optical thickness $\Lambda = 2$ and different albedos ($\omega = \rho_1 - \rho$, indicated at the left of each panel) for a bell-shaped incident laser beam with a half width at half maximum $\beta r = 1.2$.

on the width of the radial profile of the deposited energy is insignificant.

Figure 7 shows sections of computed 2D profiles. In particular, Fig. 7c presents the $r = 0$ sections of the 2D profiles displayed in Fig. 6, and Figs 7a and 7b show, respectively, the $z = 0$ and $\beta z = 2$ sections of q_z profiles, one of which is displayed at the left of Fig. 4b. The width of the radial profiles in Figs 7a and 7b is essentially independent of ρ. The energy flux across the powder surface (Fig. 7a) decreases with increasing ρ. The decrease is relatively small at the beam centre and more significant at the periphery, where there are negative flux values because the incident intensity at the periphery is lower than the backscattered intensity. This correlates with the 1D simulation results for the absorptance $A = q_z(0)$ (Fig. 3). The energy flux absorbed by the substrate surface (Fig. 7b) decreases markedly with increasing ρ. The energy deposited in the powder (Fig. 7c) also drops with increasing ρ, and its depth profile becomes more uniform.

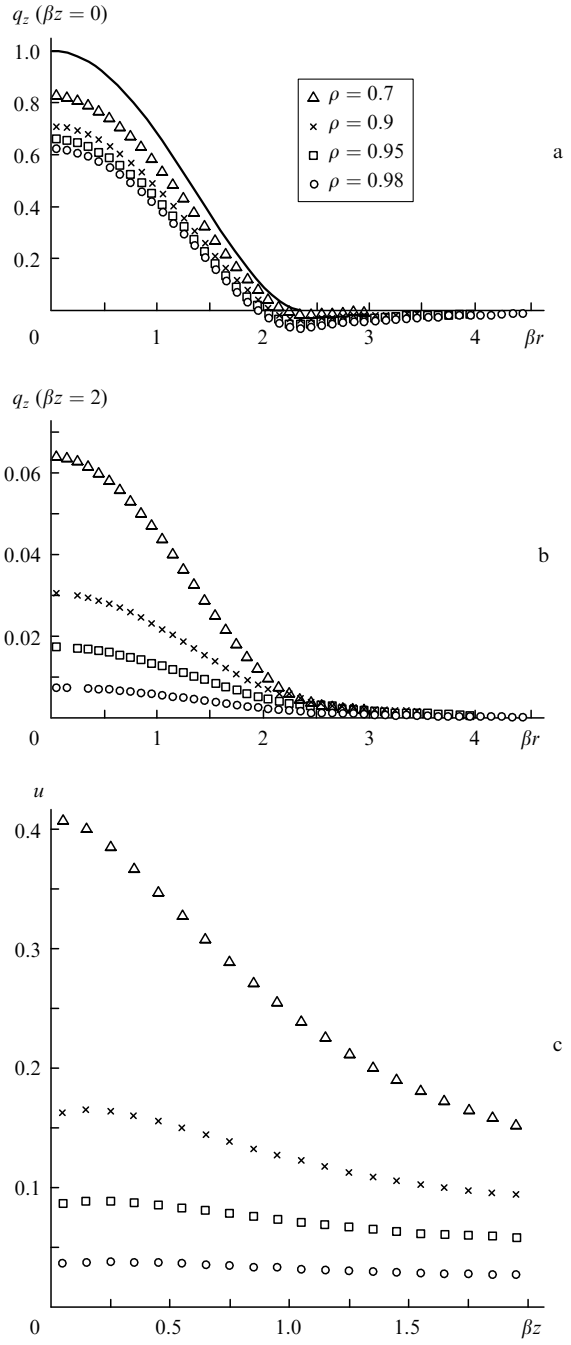

Figure 7. Comparison of the radiative transfer in powder beds of optical thickness $\Lambda = 2$ and different albedos ($\omega = \rho_1 = \rho$) for a bell-shaped laser beam with a half width at half maximum $\beta r = 1.2$: (a, b) normalised axial energy flux density, q_z, on the powder and substrate surfaces, respectively; (c) normalised absorbed energy on the axis, u. The solid line shows the radial laser beam profile.

The net energy efficiency of laser processing and the heating of the substrate decrease with an increase in the reflectance of the material, ρ. Therefore, high reflectances are usually undesirable. At the same time, the powder bed is more uniformly heated at a higher reflectance, which may be beneficial in the case of relatively thick powder beds or when overheating of the powder must be ruled out.

4. Conclusions

In the described model of radiation transfer, the absorptance of an optically thick layer of opaque powder particles is a universal function of the absorptance of the solid phase and is independent of surface area and porosity, in agreement with experimental data in the literature.

The net absorptance of the system comprising a powder layer and a substrate of the same material is an increasing function of the optical thickness of the layer and the absorptance of the solid phase. The fraction of radiation absorbed by the substrate decreases with an increase in the optical thickness of the powder layer and may have a local maximum, depending on the absorptance of the solid phase.

The radial transfer of radiant energy, due to the scattering of the incident laser radiation by the powder, may markedly reduce the energy deposition along the beam axis. The radial deposited-energy profile broadens relatively little. The maximum temperature, which occurs near the beam axis, is expected to be lowered by the radial transfer, whereas the corresponding rise in temperature beyond the beam spot will be insufficient to cause any structural or phase changes.

The fraction of laser energy absorbed in the powder-substrate system and that absorbed in the substrate decrease with an increase in the reflectance of the material, but the depth profile of the energy deposited in the powder becomes more uniform.

References

1. Santos E.C., Shiomi M., Osakada K., Laoui T. *Int. J. Mach. Tools Manuf.*, **46**, 1459 (2006).
2. Gusarov A.V., Yadroitsev I., Bertrand Ph., Smurov I. *Appl. Surf. Sci.*, **254**, 975 (2007).
3. Barnes S., Timms N., Bryden B., Pashby I. *J. Mater. Proc. Technol.*, **138**, 411 (2003).
4. Gusarov A.V., Kruth J.-P. *Int. J. Heat Mass Transfer*, **48**, 3423 (2005).
5. Rombouts M., Froyen L., Gusarov A.V., Bentefour E.H., Glorieux C. *J. Appl. Phys.*, **97**, 024905 (2005).
6. Tolochko N.K., Laoui T., Khlopkov Yu.V., Mozzharov S.E., Titov V., Ignatiev M.B. *Rapid Prototyping J.*, **6**, 155 (2000).
7. Gusarov A.V., Bentefour E.H., Rombouts M., Froyen L., Glorieux C., Kruth J.-P. *J. Appl. Phys.*, **99**, 113528 (2006).
8. Wang X.C., Laoui T., Bonse J., Kruth J.P., Lauwers B., Froyen L. *Int. J. Adv. Manuf. Technol.*, **19**, 351 (2002).

9. Van der Scheuren B. *Basic Contribution to the Development of the Selective Metal Powder Sintering Process. Ph.D. Thesis* (K.U.Leuven, Belgium,1996).
10. Rombouts M., Froyen L., Gusarov A.V., Bentefour E.H., Glorieux C. *J. Appl. Phys.*, **98**, 013533 (2005).
11. Gusarov A.V. *Phys. Rev. B*, **77**, 144201 (2008).
12. Gouttebroze P. *Astronomy Astrophys.*, **413**, 733 (2004).
13. Siegel R., Howell J.R. *Thermal Radiation Heat Transfer* (New York: Hemisphere, 1984).
14. Leveque R.J. *Numerical Methods for Conservation Laws* (Berlin: Verlag, 1992).
15. Ivanova A.M., Kotova S.P., Kupriyanov N.L., Petrov A.L., Tarasova E.Yu., Shishkovskii I.V. *Kvantovaya Elektron.*, **25**, 433 (1998) [*Quantum Electron.*, **28**, 420 (1998)].